

An extreme Ultraluminous X-ray source X-1 in NGC 5055

Samaresh Mondal ^{*}, Agata Różańska, Eleonora Veronica Lai, and Barbara De Marco

Nicolaus Copernicus Astronomical Center, Polish Academy of Sciences, ul. Bartycka 18, 00-716 Warsaw, Poland

Received XXX; accepted YYY

ABSTRACT

Aims. We analyzed multi-epoch X-ray data of the Ultraluminous X-ray source (ULX) NGC 5055 X-1, with luminosity up to 2.32×10^{40} erg s⁻¹, in order to constrain the physical parameters of the source.

Methods. We performed timing and spectral analysis of *Chandra* and XMM-Newton observations. We used spectral models which assume the emission is from an accreting black hole system. We fit the data with a multicolor disk (MCD) combined with a powerlaw (PL) or a thermal Comptonization (NTHCOMP) component, and compared those fits with a slim disk model.

Results. The lightcurves of the source do not show significant variability. From the hardness ratios (3-10 keV/0.3-3 keV flux) we infer that the source is not spectrally variable. We found that the photon index is tightly, positively correlated with the unabsorbed 0.3-10 keV flux and the hydrogen column density. Furthermore, the temperature emissivity profile indicates a deviation from the standard sub-Eddington thin disk model. The source shows an inverse correlation between luminosity and inner disk temperature in all fitted models.

Conclusions. Our analysis favors the source to be in an ultraluminous soft state. The positive correlations between the photon index and the flux, and between the photon index and the hydrogen column density may suggest the source is accreting at high Eddington ratios and might indicate the presence of a wind. The inverse luminosity relation with the inner disk temperature for all spectral models may indicate that the emission is geometrically beamed by an optically thick outflow.

Key words. Accretion, accretion disks – X-rays: individuals: NGC 5055 X-1 – Methods: data analysis

1. Introduction

Ultraluminous X-ray sources (ULXs) are off-nuclear point sources with isotropic X-ray luminosity in excess of 10^{39} erg s⁻¹ (Fabbiano 1989). Due to their high luminosity ULXs were suggested to host an intermediate mass black hole (IMBH, Colbert & Mushotzky 1999); however, the recent discovery of coherent pulsations showed that some ULXs contain a neutron star (Bacchetti et al. 2014; Fürst et al. 2016, 2017; Israel et al. 2017a,b; Carpano et al. 2018). This finding was independently confirmed in three sources, through fitting with a spectral model which assumes non-isotropic emission from a neutron star - accretion disk system (Różańska et al. 2018). ULXs are also exciting in the context of gravitational wave studies. Some ULXs have a high mass donor (Motch et al. 2011, 2014; Heida et al. 2015, 2016) that might eventually result in the merging of two compact objects at the end of its stellar evolution (Mondal et al. 2020).

As most ULXs are extra-galactic sources, the direct measurement of the mass of the compact object is extremely difficult. Therefore, we have to rely on indirect methods, like BH mass-scaling of the inner disk temperature ($T_{\text{in}} \propto M^{-1/4}$) (Miller et al. 2003). Most ULX spectra are fitted with two components model: a multicolor accretion disk model (hereafter MCD) and a hard powerlaw (hereafter PL) tail. Fitting of this model to many ULX spectra results in very cool inner disk temperature, $kT_{\text{in}} \sim 0.1 - 0.3$ keV and a PL tail $\Gamma \sim 1.5 - 3$ (Kaaret et al. 2003; Miller et al. 2004a,b). If this temperature corresponds to the temperature at the inner disk radius, then the inferred BH mass would be $\sim 10^3 M_{\odot}$. This supports the IMBH interpretation with sub-Eddington accretion rate, although ULXs spectra do

not clearly resemble the typical low/hard or high/soft state spectra of BH X-ray binaries (BHXBs). However, studies of Galactic BHXBs showed that the derived temperature from the disk component is reliable only when the spectrum is dominated by the disk emission (Done & Kubota 2006). As the contribution from the PL tail component becomes significant the derived disk temperature is extremely unreliable.

ULXs have been observed to show various types of spectral shapes. High quality XMM-Newton data revealed spectral curvature associated with the hard X-ray emission component in the 2-10 keV band (Stobbart et al. 2006; Gladstone et al. 2009; Kajava et al. 2012). Fits with phenomenological spectral models allowed for the identification of four main types of spectral shapes: soft ultraluminous, hard ultraluminous, broadened disk and super soft ultraluminous. These four types have been ascribed to different accretion regimes (for more details see Kaaret et al. 2017, and references therein).

King et al. (2001) suggested that most ULXs have a stellar mass compact object accreting at super-Eddington rate and their high luminosity results from the beaming of the X-ray emission due to a geometrically thick wind outflowing from the disk. Fitting of some ULX spectra with MCD plus PL components, Feng & Kaaret (2007) and Kajava & Poutanen (2009) found that the temperature of the soft component is inversely correlated with luminosity $L \propto T^{-3.5}$, which is at odds with the $L \propto T^4$ relation expected from theory and observed in BHXBs (Gierliński & Done 2004). King & Puchnarewicz (2002) showed that this inverse relation is actually expected when the source is beamed and accreting at super-Eddington rate. Motivated by the observed soft temperature-luminosity relation King (2009) derived an empirical relation describing the scaling of the beaming factor with the inverse of the square of the accretion rate, which implies

^{*} E-mail: smondal@camk.edu.pl (SM)

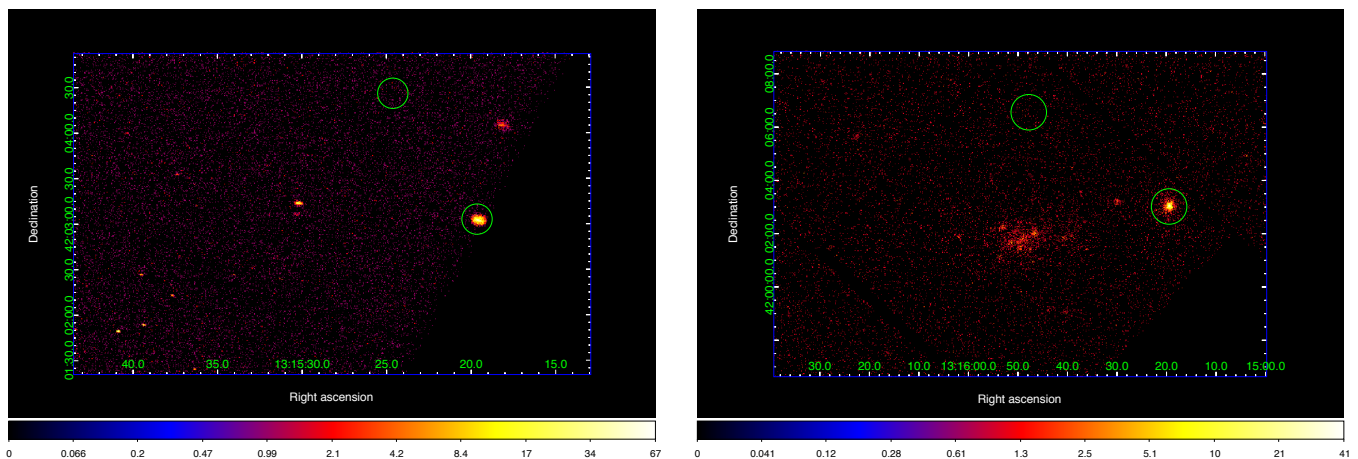


Fig. 1: The X-ray image in counts/pixel displays the field of view of *Chandra* ACIS-S (left panel) and XMM-Newton EPIC-MOS1 (2007–05–28; right panel) detectors. The green circles containing bright pixels show NGC 5055 X-1, while the empty green circles represent the region from where the background was extracted. *Chandra* spatial resolution allowed us to extract source photons from a circular region of 6'' radius, while for XMM-Newton we used circular regions of 40''.

Detector	Mission ObsID	Date	GTI [ks]	Net total Counts
<i>Chandra</i>				
ACIS-S	2197	2001.08.27	28.3	2283
XMM-Newton				
MOS1			10.9	1272
MOS2	0405080301	2007.05.28	10.9	1336
PN			8.9	4016
XMM-Newton				
MOS1			16.1	1224
MOS2	0405080501	2007.06.19	7.8	705
PN			3.05	1149

Table 1: Details of X-ray observations analyzed in this paper. The detectors used are listed in column 1, observation ID given in column 2, date given in column 3. The exposure good time intervals (GTI), and the net total counts are listed in column 4 and 5 respectively.

that the most luminous ULXs are highly collimated. However, in the presence of a powerful disk wind one would expect that at large distances from the BH the wind becomes optically thin, and emission and/or absorption lines associated with radiation passing through the partially ionized optically thin phase of the wind can be observed. Such features have been found in recent studies of NGC 5408 X-1 and NGC 6946 X-1 by Middleton et al. (2014), and of NGC 1313 X-1 and NGC 5408 X-1 by Pinto et al. (2016).

Here, we report on the analysis of *Chandra* and XMM-Newton observations of an extreme ULX in the outskirts of the spiral galaxy NGC 5055 (M63). The source NGC 5055 X-1, was serendipitously discovered by *ROSAT* High Resolution Imager (HRI) (Roberts & Warwick 2000). Follow-up observations were carried out by *Chandra*, XMM-Newton and *Swift*. In spite of being very luminous in the X-ray band, reaching $\sim 2.3 \times 10^{40}$ erg s $^{-1}$ (Swartz et al. 2011), the source has received very little attention and none of the available X-ray observations are reported in the literature.

In this paper, we perform the first systematic analysis of X-ray observations of NGC 5055 X-1, using three longest *Chandra*

and XMM observations. We carried out X-ray timing and spectral analysis, using phenomenological models available in *xSPEC* fitting package (Arnaud 1996). The data reduction process is presented in Sec. 2. The timing and spectral analysis are presented in Secs. 3 and 4, respectively. The most important correlations between physical parameters are shown in Sec. 5 and the conclusions are reported in Sec. 6.

2. Observations and data reduction

The source NGC5055 X-1 is located at R.A. = 13^h15^m19.54^s and decl. = 42°03'02.3". The distance to the galaxy was reported to be 9.2 Mpc (Tully et al. 2013; Tikhonov et al. 2015; McQuinn et al. 2017), and we use this value throughout this paper. There are many observations of NGC 5055 X-1 by several X-ray observatories, but most of them are short observations with not enough counts for a meaningful spectral analysis. Most of the *Swift* observations have exposure time $\lesssim 10.0$ ks, and total counts ~ 160 . The only three long observations available are from *Chandra* ACIS-S and XMM-Newton EPIC-MOS1, MOS2, and EPIC-PN, with a total of ~ 1000 net counts, which we used in this study. The details of these observations are given in Tab. 1.

For the data reduction, standard procedures were followed, as described in detail in the following subsections. In all cases NGC5055 X-1 was located in the field of view, but close to the edge of the chip, as shown in Fig. 1, where the X-ray images of the source from both satellites are presented.

2.1. Chandra data

We reduced the data from the ACIS-S detector using the standard pipeline *Chandra* Interactive Analysis software CIAOv4.12. NGC 5055 X-1 was detected close to the edge of the field of view (see left panel of Fig. 1), while the observatory pointed at the center of NGC 5055. We used *chandra_repo* to remove the hot pixels, creating new event files and producing good time intervals. The source and background were extracted from a circular region of 6'' radius as shown in Fig. 1 left (green circles). The background-subtracted source lightcurve was created using *dmextract*. The spectrum was generated using *specextract*

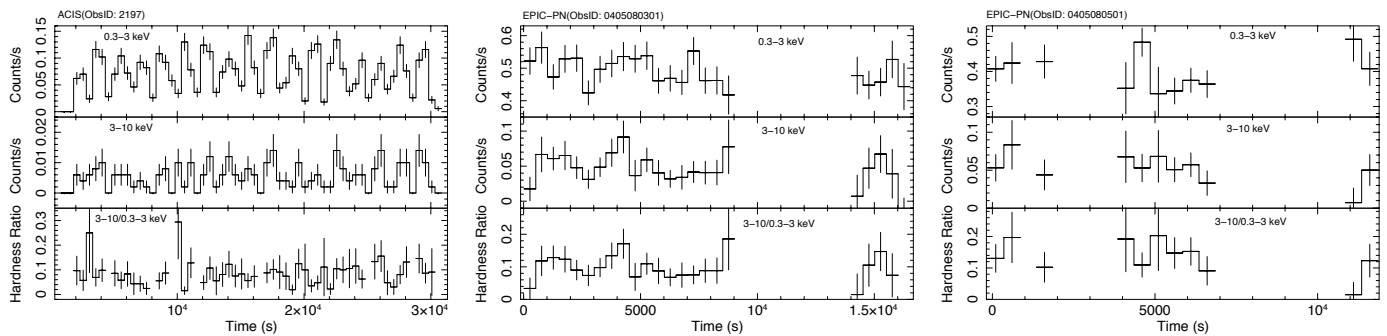


Fig. 2: The *Chandra* ACIS-S and XMM-Newton EPIC-PN lightcurves of NGC 5055 X-1 for the three observations at different epochs (the observation IDs are indicated in each panel). Soft 0.3-3 keV and hard 3-10 keV energy band lightcurves are shown in the upper and middle panels respectively, while - bottom panels show the hardness ratios for each set of data. All the lightcurves are re-binned with bin size 500 s to have higher signal to noise ratio. The zero times in the plots correspond to 2001–08–27 02:13:48, 2007–05–28 07:59:14, and 2007–06–19 10:56:29 for panels from left to right, respectively.

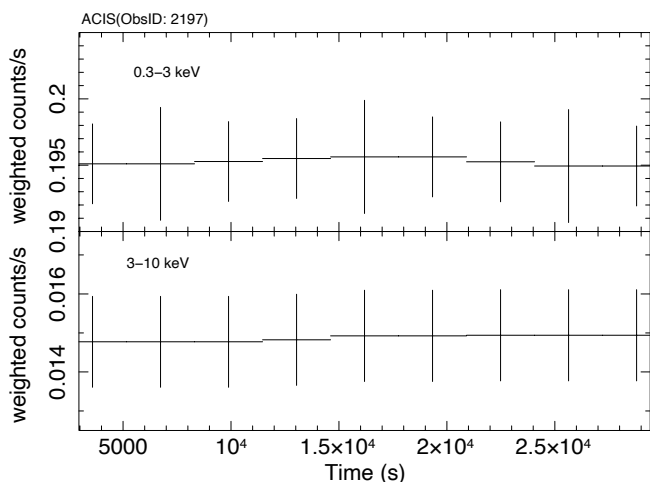


Fig. 3: The *Chandra* observation probability-weighted lightcurves, as obtained from the CIAO `glvary` tool, i.e. after taking account all instrumental effects. The zero time corresponds to 2001–08–27 02:13:48. The total probability of variability for the 0.3-3 keV and 3-10 keV lightcurves is 0.02 and 0.07, respectively (see Sec. 3).

taking into account the correction for the point spread function (PSF) for off-axis sources. The auxiliary files and redistribution matrices were generated with `specextract` using the module `mkarf` and `mkrmf`, respectively. Given that NGC 5055 X-1 is close to the chip edge (see Fig. 1), the spacecraft dither may cause the temporal disappearance of the source from the field of view. We have taken this into account in our timing analysis (see Sec. 3), and when making auxiliary files for spectral analysis.

2.2. XMM-Newton

The data reduction was done using XMM-Newton Science Analysis System (SASv16.0.0) following standard procedures. The observation data files (ODF) were processed using `emproc` and `epproc` to create calibrated event lists for EPIC-MOS and EPIC-PN detectors, respectively. A circular region of 40'' radius was chosen to extract source and background counts. We used `evselect` to generate lightcurves and spectra selecting single and double events for EPIC-PN detector and single to quadruple events for EPIC-MOS detector. The source lightcurve was corrected from background counts using `epic1ccorr`. The auxiliary files and redistribution matrices were generated using

`arfgen` and `rmfgen`. We note that for XMM-Newton observation in 2007 June, the EPIC-MOS and EPIC-PN were not observing strictly simultaneously. There is a ~ 52 minutes of delay between the start times of EPIC-MOS and EPIC-PN, which results in a shorter effective (after removing periods of flaring background) exposure time for EPIC-PN, as listed in Tab. 1.

3. Timing analysis

The main purpose of our timing analysis is to find out if the source shows significant temporal and spectral variability. We used *Stingray*¹ (Huppenkothen et al. 2019) in order to construct power spectral density (PSD) from the extracted lightcurves. *Stingray* is an open source spectral-timing Python software package for astrophysical data analysis.

We used the XMM-Newton EPIC-PN lightcurves for timing analysis as the EPIC-PN detector has higher full frame time resolution (73.4 ms) and effective area than the EPIC-MOS cameras. The lightcurves were extracted with a time bin of 0.22 s (3 times the temporal resolution) to have enough counts in each bin. We used 9.6 s time bin (*Chandra* temporal resolution is 3.2 s) to extract the lightcurves from *Chandra* ACIS-S observation. Fig. 2 shows the ACIS-S and EPIC-PN lightcurves for the two bands 0.3-3 keV and 3-10 keV, re-binned with bin size 500 s. We do not show lightcurves from both MOS cameras in the figure due to their lower S/N ratios. The source does not display either flux nor spectral variability.

Nonetheless, ACIS-S lightcurves show enhanced variability with an apparently quasi-periodic pattern. The hardness ratios are consistent with being constant (left most panel of Fig. 2). We constructed PSD from ACIS-S lightcurves to explore the nature of the periodic pattern. To this aim, we used the unbinned lightcurves, with a time resolution of 9.6 s. Each individual lightcurve was divided into 4 segments and the PSD was computed in each segment separately. Then, we averaged the PSD from the 4 segments.

In *Chandra* data we found periodic variations corresponding to two peaks at 1.4 mHz and 2.8 mHz. Such features are clearly not observed during XMM observations. While the hypothesis of a quasi-periodic feature in *Chandra* lightcurves disappearing in later XMM observations is tantalizing, we verified this is most likely an instrumental artifact. Indeed, as pointed out in Sect. 2.1, the satellite dithering motion combined with the position of

¹ <https://stingray.readthedocs.io/en/latest/>

Data	N_{H}	kT_{in}	p	Γ	kT_{e}	$F_{(0.3-10)\text{keV}}$	$L_{(0.3-10)\text{keV}}$	χ^2_{red}
Model	$10^{20} [\text{cm}^{-2}]$	[keV]			[keV]	[erg s $^{-1}$ cm $^{-2}$]	[erg s $^{-1}$]	
2001.08.27								
TBNEW*(MCD+PL)	$15.18^{+1.96}_{-1.73}$	$0.21^{+0.02}_{-0.04}$		$2.40^{+0.12}_{-0.11}$		2.30×10^{-12}	2.32×10^{40}	1.22
TBNEW*(DISKPBB)	$8.30^{+1.86}_{-1.62}$	$1.27^{+0.25}_{-0.17}$	$0.50^{+0.03}_{-0.01}$			1.67×10^{-12}	1.68×10^{40}	1.25
TBNEW*(MCD+NTHCOMP)	$3.86^{+1.90}_{-1.66}$	$0.22^{+0.01}_{-0.02}$		$2.21^{+0.15}_{-0.12}$	$1.62^{+0.95}_{-0.95}$	1.40×10^{-12}	1.41×10^{40}	1.21
2007.05.28								
TBNEW*(MCD+PL)	$7.76^{+0.88}_{-0.82}$	$0.24^{+0.01}_{-0.01}$		$1.99^{+0.08}_{-0.08}$		1.55×10^{-12}	1.57×10^{40}	1.09
TBNEW*(DISKPBB)	$5.06^{+0.84}_{-0.77}$	$1.98^{+0.46}_{-0.30}$	$0.50^{+0.02}_{-0.01}$			1.33×10^{-12}	1.34×10^{40}	1.22
TBNEW*(MCD+NTHCOMP)	$3.72^{+0.87}_{-0.80}$	$0.25^{+0.004}_{-0.005}$		$1.85^{+0.09}_{-0.07}$	$1.78^{+1.56}_{-0.40}$	1.28×10^{-12}	1.29×10^{40}	1.08
2007.06.19								
TBNEW*(MCD+PL)	$7.60^{+1.51}_{-1.34}$	$0.26^{+0.01}_{-0.01}$		$1.75^{+0.12}_{-0.11}$		1.17×10^{-12}	1.18×10^{40}	1.12
TBNEW*(DISKPBB)	$5.98^{+1.42}_{-1.26}$	$2.86^{+0.67}_{-0.67}$	$0.50^{+0.03}_{-0.01}$			1.04×10^{-12}	1.05×10^{40}	1.22
TBNEW*(MCD+NTHCOMP)	$5.53^{+1.51}_{-1.34}$	$0.27^{+0.006}_{-0.006}$		$1.59^{+0.10}_{-0.07}$	$1.62^{+0.60}_{-0.28}$	1.02×10^{-12}	1.03×10^{40}	1.12

Table 2: Best fit parameters obtained from the fits of each set of data. We tied the disk inner radius temperature to the temperature of the soft seed photons for thermalized Compton emission in MCD+NTHCOMP model. For XMM-Newton observations MOS1, MOS2 and PN data were fitted simultaneously. The unabsorbed flux and luminosity in the range 0.3-10 keV estimated from the best-fit model are given in column 7 and 8, assuming a distance to the source of 9.2 Mpc.

the source near the edge chip, may cause the source to periodically disappear. To verify this, we used the CIAO tool `glvary` to search for significant variability in *Chandra* lightcurves. The `glvary` tool utilizes information from the `dither_region` tool to correct the instrumental effects. The `dither_region` tool calculates the fractional area of the source region as a function of time that takes into account for the corrections for chip edges, bad pixels, and bad columns. As an output, `glvary` computes the probability that the lightcurve is variable using Gregory-Loredo algorithm (Gregory & Loredo 1992). The resulting probability values for the 0.3-3 keV and 3-10 keV lightcurves are 0.02 and 0.07, implying that the source is not significantly variable. In Fig. 3, the *Chandra* probability-weighted lightcurves obtained with `glvary` are presented. We conclude that the source is not significantly variable and the quasi-periodic feature is an instrumental artifact. A more detailed description on how the dither motion affects the observed lightcurves for sources located near the chip edge is given in Roberts et al. (2004).

4. Spectral analysis

As the hardness ratios presented in Figs. 2 and 3 (lowest panels) do not show significant indications of spectral variability, we carried out fits to the time-averaged spectra of the single observations. We tested simple accretion disk models in order to understand the basic properties of the source. We utilized the `xSPEC`12.10.1 (Arnaud 1996) software for spectral analysis and different spectral models were used to fit the data: we first fit a simple MCD using the DISKBB model in `xSPEC`, then we added a POWERLAW component (MCD+PL); next we considered slim disk emission (DISKPBB model, Mineshige et al. 1994; Hirano et al. 1995; Watarai et al. 2000; Kubota & Makishima 2004; Kubota et al. 2005); and finally we considered a thermal Comptonization component due to a hot corona (MCD+NTHCOMP, Zdziarski et al. 1996; Życki et al. 1999). The spectra are fitted in the band 0.3-10 keV and re-binned to have minimum of

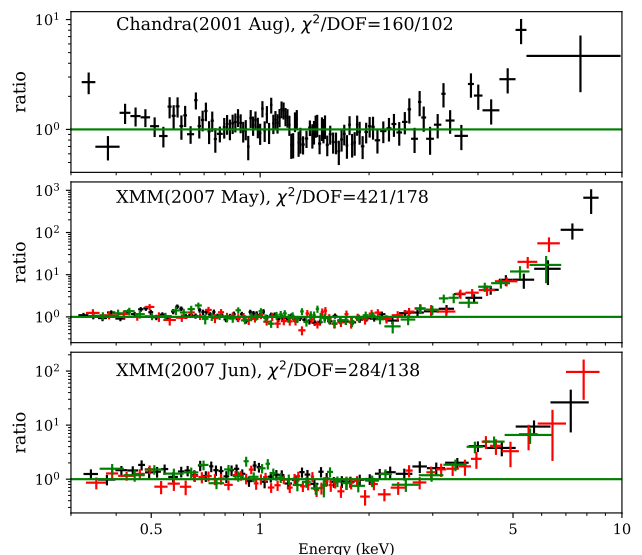


Fig. 4: The ratio of data to folded model obtained from the fit of a MCD model, using DISKBB in `xSPEC`. The MCD model clearly leaves an excess at high energies. In XMM-Newton panels the black, red and green data points are, respectively, the EPIC-PN, EPIC-MOS1 and EPIC-MOS2 spectra.

20 counts in each energy bin. The effect of interstellar absorption was accounted for using TBNEW². We let the hydrogen column density N_{H} free to vary, and keeping in mind that the value of Galactic absorption towards NGC 5055 is estimated to be $\sim 3.57 \times 10^{20} \text{ cm}^{-2}$ (HI4PI Collaboration et al. 2016).

Following standard recommendations (see SAS website³), we did not co-add the spectra from each XMM-Newton detec-

² <https://pulsar.sternwarte.uni-erlangen.de/wilms/research/tbabs/>

³ <https://www.cosmos.esa.int/web/xmm-newton/sas-thread-epic-merging>

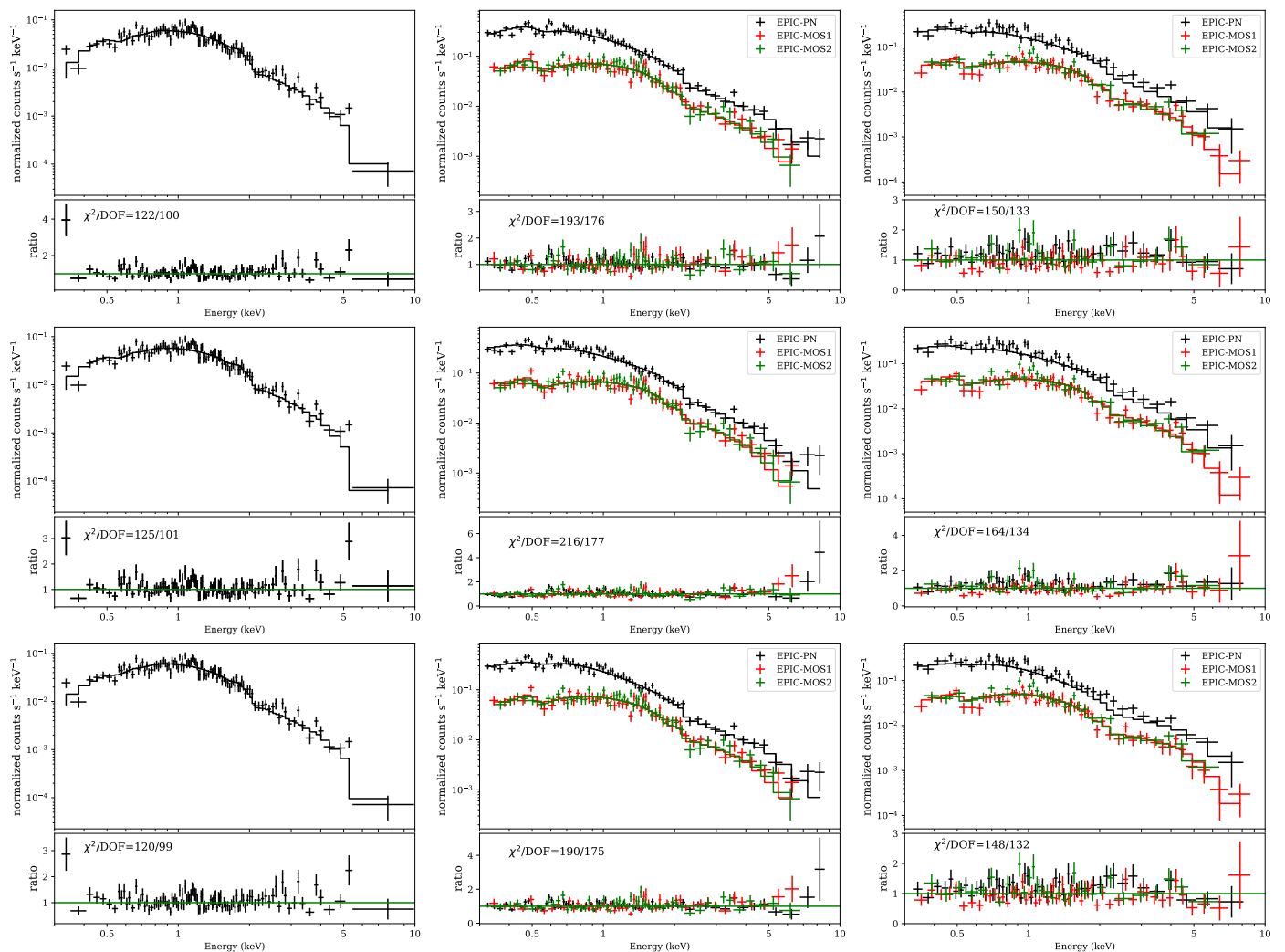


Fig. 5: Each subplot shows the data with the folded model in the upper panel, and the data-to-model ratio in the lower panel. In the first row, the results from the fit of the MCD+PL model are presented, in the second row - DISKPB model, and finally in the third row - MCD+NTHCOMP. The different columns correspond to *Chandra* data - left column, XMM-Newton 2007–05–28 data - middle column, and 2007–06–19 data - right column.

tor, but we fit them simultaneously. We used the same models for *Chandra* and XMM-Newton data sets, and as a result we obtained constraints on physical parameters from three different epochs.

As a first step, we tested the well known MCD model, representing emission from a standard Shakura & Sunyaev (1973) thin disk. The standard disk model is appropriate when the source accretion rate is below the Eddington value, assuming that the accretion disk is geometrically thin ($h/r \ll 1.0$) and the radiation is emitted locally as black body from optically thick gas. When we fit each data set with a single MCD, the reduced χ^2 is high, and the ratio of data to the model significantly differs from unity as shown in Fig. 4. Furthermore, the best-fit N_H value is very low, much lower than the estimated value for Galactic absorption, which suggests that the fit is unphysical.

Adding an extra PL component to the MCD model, we obtained an excellent fit for all the three data sets, as described in Tab 2 and shown in Fig. 5 (upper panels). The inner accretion disk temperature is relatively low compared to the values typically observed in Galactic BHXBs in the soft state (Gierliński & Done 2004). Assuming the source is in a state similar to the soft state, then the low temperature is consistent with an IMBH

of $\sim 10^3 M_\odot$. The first XMM-Newton data set (2007–05–28) has higher flux than the second data set (2007–06–19), but slightly lower than in *Chandra* data. The required Galactic N_H in *Chandra* is twice as large than in both XMM-Newton data sets.

However, the assumption of a geometrically thin and optically thick disk is not valid when the source is close or above the Eddington limit. The luminosity of NGC 5055 X-1 is very high. If the accretor is a stellar mass BH, then the accretion rate is well above the Eddington rate. Assuming a $10 M_\odot$ BH and isotropic emission we infer $\dot{M}_{\text{acc}} > 10^4 \dot{M}_{\text{Edd}}$, and bolometric luminosity as:

$$L_{\text{bol}} = L_{\text{Edd}} [1 + \ln(\dot{M}_{\text{acc}}/\dot{M}_{\text{Edd}})]. \quad (1)$$

In the regime of super-Eddington accretion, the disk becomes geometrically thick ($h/r \sim 1$) and the photon diffusion timescale in the vertical direction becomes much longer than the radial infall timescale. This allows some of the photons to be advected radially into the BH rather than emitted locally which leads to a flatter effective temperature profile (Abramowicz et al. 1988; Watarai et al. 2000). The high luminosity of NGC 5055 X-1 suggests that the accretion rate may be extremely high. In this

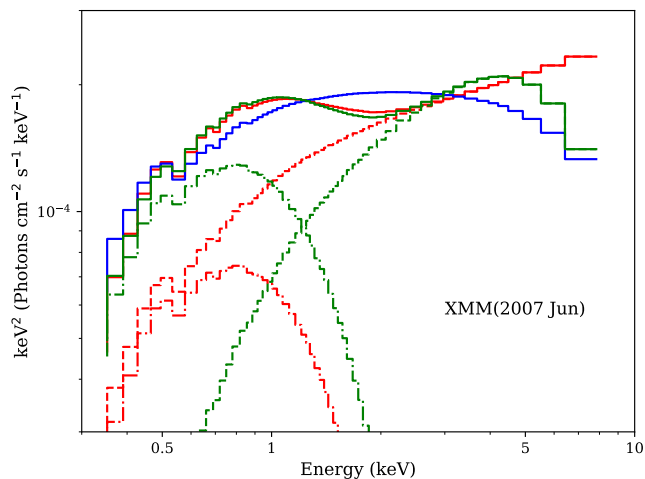


Fig. 6: Unfolded absorbed models (solid lines) and model components (dot-dashed line for MCD and dashed line for NTHCOMP and PL) fitted to the XMM-Newton 2007–06–19 data. Red lines represent the MCD+PL model, the blue line is the DISKPB model, and green lines show the MCD+NTHCOMP model in which the MCD component is the most prominent.

case one would expect a significantly different temperature profile than in the standard thin disk model. The DISKPB slim disk model allows the disk radial temperature profile to be fit to the data, with the local disk temperature $T(r) \propto r^{-p}$, where p is a free parameter. The standard MCD model is recovered if $p = 0.75$ and has been usually used in previous studies of ULXs.

The DISKPB model while providing an overall acceptable description of the data, yields slightly worse fits, as shown in Fig. 5 middle row panels. All best-fit parameters are described in Tab. 2. The Galactic N_{H} is lower than in the case of MCD+PL model giving higher inner disk temperature, i.e. $kT_{\text{in}} = 1.27, 1.98$ and 2.86 keV for the first, second and third data set, respectively. The temperature profile obtained from this model is the same in all data sets i.e. $T(r) \propto r^{-0.5}$ which is significantly different from the thin disk model ($p = 0.75$).

The fit with MCD+NTHCOMP model presented in Fig. 5 bottom panels, gives the same reduced χ^2 and the same disk T_{in} as the MCD+PL model (see Tab. 2 for details). The only difference is the value of Galactic absorption, which in the case of the MCD+NTHCOMP model has lower values than in other models, but in agreement with independent measurements of N_{H} (as reported by HI4PI Collaboration et al. 2016), for the first two data sets. This means that the normalization, and hence the contribution, of the MCD component is higher when fitted together with the NTHCOMP component than with a simple PL component, as illustrated in Fig. 6. Even if the fit statistic does not allow us to differentiate between those two models, the inferred value of Galactic absorption slightly favors the MCD+NTHCOMP model. The second reason to favor the model with thermal Comptonization is that in this model the two components are physically linked in a self-consistent way, i.e. the temperature of the corona and hence the low energy cut-off of NTHCOMP depends on the inner disk temperature. On the contrary, the PL component does not have a low energy cut-off, and therefore the model is less physical. The temperature of the corona from the MCD+NTHCOMP best-fit model is quite low $kT_{\text{e}} \sim 1.68 - 1.78$ keV. This is commonly observed in ULXs (Gladstone et al. 2009) and can be ascribed to a cool corona,

reminiscent of the soft X-ray excess often observed in some BH accreting sources (Gronkiewicz & Rózańska 2020; Petrucci et al. 2020, and references therein).

All models give unabsorbed X-ray flux in the 0.3-10 keV band, within the range $1.0-2.3 \times 10^{-12}$ erg s $^{-1}$ cm $^{-2}$, as reported in Tab. 2. Considering a distance of 9.2 Mpc to NGC 5055, these correspond to an isotropic luminosity in the range $1.1-2.3 \times 10^{40}$ erg s $^{-1}$ as listed in Tab. 2. Sources in the luminosity range $10^{40} - 10^{41}$ erg/s are classified as extremely luminous X-ray source (ELX) (Devi et al. 2007; Singha & Devi 2019). An ELX resembles the so called ultraluminous (UL) spectral state (Sutton et al. 2013). UL hard states (dominated by emission from a hot corona) and UL soft states (dominated by emission from a cool corona) have been observed (Gladstone et al. 2009). From the data of NGC 5055 X-1 it is not possible to clearly discern whether the source might be in a UL hard state, which is characterized by a hard powerlaw, or in a UL soft state, in which the power law shows a cut-off at lower energies. Given the inferred best-fit electron temperatures, the slightly favoured MCD+NTHCOMP model suggests the source to be in a UL soft state.

To illustrate this issue, in Fig. 6 we plotted the unfolded models for one XMM-Newton observation (2007–06–19). From a statistical point of view those models do not differ much, but our previous considerations regarding the N_{H} favour the MCD+NTHCOMP model. Longer observations, extending to hard X-ray energies (e.g. by NuSTAR) are needed to better resolve the high energy tail and confirm this interpretation.

5. Discussions

Our spectral analysis shows three possible phenomenological models for the spectra of NGC 5055 X-1. The spectral models assume the emission is from an accreting BH system. All the three models can describe the data well from a statistical point of view. The results obtained from spectral fitting can be used to search for correlations between parameters. In case of the MCD+PL model we found a strong correlation between the unabsorbed flux in the range 0.3-10 keV, and the photon index Γ , with correlation coefficient 0.99, as shown in Fig. 7 (blue points and line). The correlation coefficient was measured using the Pearson product-moment. This correlation shows that the higher the flux the steeper the hard X-ray spectrum, as typically seen in BHBs above 0.5-1 percent of the Eddington accretion rate (Skipper & McHardy 2016). A similar behaviour was found with correlation coefficient 0.86 in NGC 1313 X-1, 0.91 in NGC 1313 X-2 (Feng & Kaaret 2006b), 0.99 in NGC 5204 X-1 (Feng & Kaaret 2009) and in many other ULXs (Feng & Kaaret 2006a; Kajava & Poutanen 2009).

Following the studies of Gladstone et al. (2009) on a large sample of ULXs, we fit the data also with a MCD+PL model. As found by Feng & Kaaret (2009) for NGC 5204 X-1 using the same MCD+PL model, we also found a correlation between N_{H} and Γ with correlation coefficient 0.93, as shown in Fig. 7 (red points and line). The correlation shows that as Γ increases (simultaneously with the flux) the N_{H} also increases. If this correlation is intrinsic, this might imply that an increase of flux leading to strong outflows from the disk, which in turn results in an increase of the hydrogen column density of the disk wind. An additional argument for the possible existence of a wind is that the total hydrogen column density obtained from all our MCD+PL model fits is at least two times higher than the Galactic value for this source (see Sec. 4). This might be the evidence of additional intrinsic absorption connected to the source. Nevertheless,

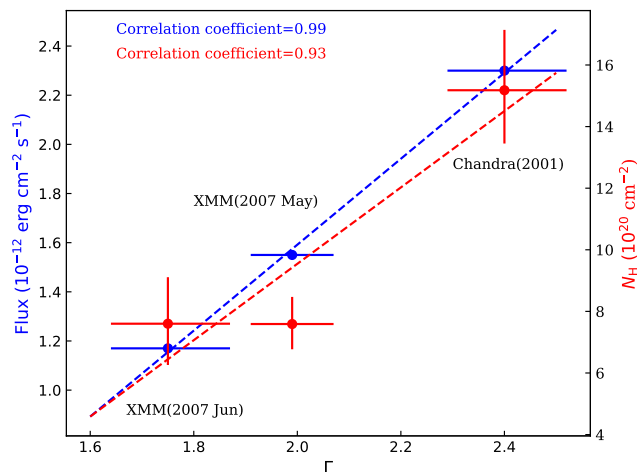


Fig. 7: The unabsorbed 0.3-10 keV flux and hydrogen column density versus photon index obtained from MCD+PL model fit. The correlation between $F_{(0.3-10)\text{keV}}$ and Γ is shown in blue, while correlation between N_{H} and Γ is shown red. The data points were fitted with a linear model and the best-fit model is represented by the dashed lines in the plot.

a confirmation of the presence of a wind in NGC 5055 X-1 can only come from the analysis of high spectral resolution data from the Grating spectrometers on *Chandra* and XMM-Newton. We considered available archival data from XMM-Newton reflection gratings (RGS), but the exposure time is too short to obtain any significant detection of emission and absorption lines in NGC 5055 X-1.

In general, the DISKPB model gives higher inner disk temperature than the MCD+PL model. The important point to note is that we found $T(r) \propto r^{-0.5}$ in all our data sets which is flatter than expected for a sub-Eddington accretion disk model. Although the source luminosity changes during different epochs of observations, the temperature profile does not respond to such variations (the best-fit values of p are constant). Feng & Kaaret (2007) performed a similar modeling of NGC 1313 X-2 with p as a free parameter, they also obtained high inner disk temperature and $p \sim 0.5$. This fact can indicate that the disk in ULX sources may be slim, but a definite answer can come only from a systematic fit of a sample of sources using this model.

The inner temperature T_{in} , inferred from MCD+PL and MCD+NTHCOMP models is relatively low in comparison with the temperature from the DISKPB model. We plot the luminosity versus T_{in} for the three models in Figs. 8, 9 and 10. It is clear that NGC 5055 X-1 follows an inverse relation of luminosity with T_{in} for all models. The inferred relation is $L \propto T_{\text{in}}^{-(3.14^{+1.07}_{-1.51})}$ for the MCD+PL model, $L \propto T_{\text{in}}^{-(0.57^{+0.14}_{-0.08})}$ for the DISKPB model, and $L \propto T_{\text{in}}^{-(1.45^{+0.25}_{-0.46})}$ for the MCD+NTHCOMP model. This negative correlation is one of the signatures that the emission from the source is geometrically beamed as argued by King (2009). Feng & Kaaret (2007) and Kajava & Poutanen (2009) showed that for powerlaw type ULXs the soft-bump follows the relation $L \propto T_{\text{in}}^{-n}$ where $n \approx 3.5$. Among our fits, the MCD+PL follows more closely the predicted $n \approx 3.5$ trend, although a negative trend is seen in all the other fits. The errors on the inferred relations account for the quite large errors on the temperature. Even considering these errors, the slope of the correlation remains negative, regardless of the model. Of course, the quality

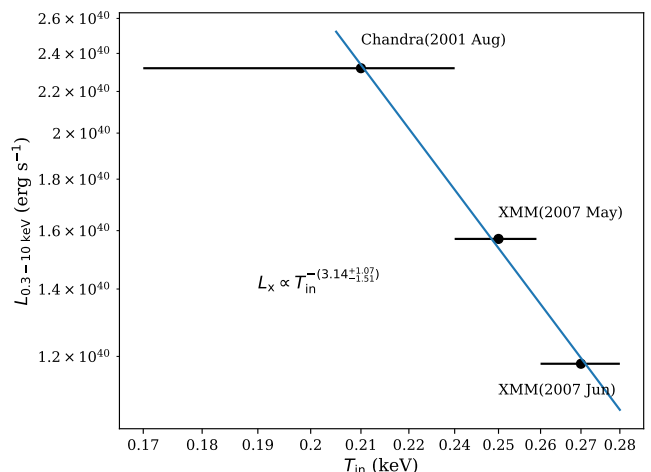


Fig. 8: Unabsorbed X-ray luminosity – inner disk temperature relation inferred from the fit of the MCD+PL model. The blue continuous line shows the best fit to the data which follows the relation $L_{(0.3-10)\text{keV}} \propto T_{\text{in}}^{-3.14}$.

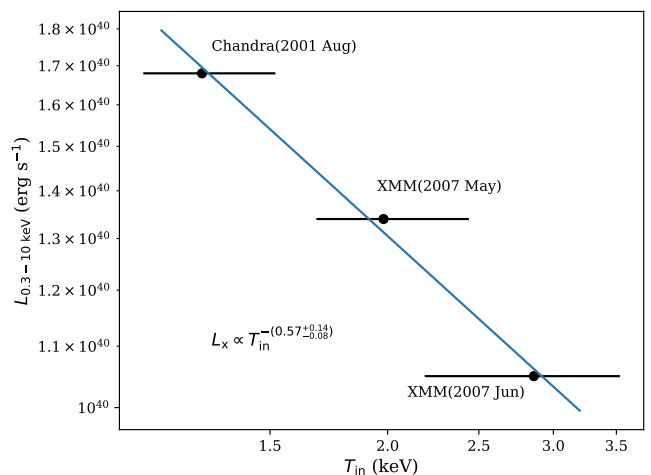


Fig. 9: Unabsorbed X-ray luminosity – inner disk temperature relation inferred from the continuum fitting using slim accretion disk DISKPB model. The blue continuous line shows the best fit to the data which follows the relation $L \propto T_{\text{in}}^{-0.57}$.

of the data and the small number of data points precludes us from obtaining stronger constraints. A longer monitoring is needed to distinguish among the different models and confirm these conclusions.

6. Conclusions

We have analyzed the *Chandra* and XMM-Newton observations of the ULX NGC 5055 X-1. The high luminosity of the source most likely results from the combination of super-Eddington accretion and geometrical beaming. The source does not show much variability in all the three observations. Although the quality of the data does not allow us to draw strong conclusions, our spectral fits hint at interesting results and trends.

(i) NGC 5055 X-1 mostly emits in soft X-rays in the range of 0.3-3 keV, and the hard X-ray band flux is only a fraction 0.1-0.3 of the soft X-ray emission, suggesting a dominant thermal

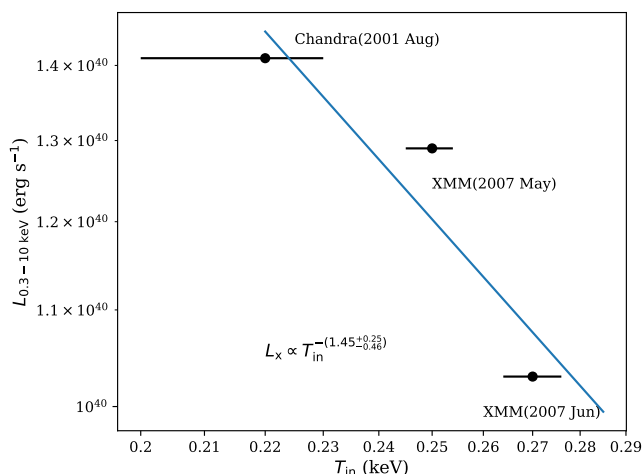


Fig. 10: Unabsorbed X-ray luminosity – inner disk temperature relation inferred from the fit of the MCD+NTHCOMP model. The blue continuous line shows the best fit to the data which follows the relation $L \propto T_{in}^{-1.45}$.

component. Therefore, we tested models of emission from an accretion disk around a BH.

(ii) The low inner disk temperature ($kT_{in} \sim 0.25$ keV) and the steep power law slope ($\Gamma > 1.5$) obtained in some fits may suggest an IMBH. On the other hand the slim disk model DISKPB provides a good fit, and suggests a temperature emission profile $T(r) \propto r^{-0.5}$, which is at odds with that of standard thin disk models (Feng & Kaaret 2007).

(iii) All unabsorbed models confirm that NGC 5055 X-1 is intrinsically extremely luminous, reaching 0.3-10 keV luminosity of 2.32×10^{40} erg s⁻¹. Our analysis slightly favors the source to be in a soft UL spectral state, but we need better data with longer exposure time to fully confirm this conclusion.

(iv) The flux and N_H are positively correlated with the photon index Γ for the MCD+PL model. The source jumps from a steep PL ($\Gamma \approx 2.4$) state to a hard PL state ($\Gamma \approx 1.8$), while N_H varies between $\sim 6 - 16 \times 10^{20}$ cm⁻². This correlation may suggest that the accretion geometry is disk+corona (Cao 2009, and references therein). The increasing absorption column density of hydrogen can be interpreted as an outflow from the disk.

(v) From a physical point of view, the MCD+NTHCOMP model is slightly more favored, since it returns a value of N_H consistent with that determined in previous measurements, and it allows for a more physical dependence between the two spectral components.

(vi) For all models we find an inverse relation of X-ray luminosity with inner disk temperature. The errors on the temperature are quite large, but regardless of the fitted model, the slope of this correlation is consistent with being negative within the estimated errors. This result strongly suggests that the source is geometrically beamed. Therefore, we conclude that a plausible explanation for NGC 5055 X-1 is that the source is accreting at super-Eddington luminosity, and is beamed by an optically thick wind, as seen in other high luminosity ULXs (King 2009).

Further simultaneous broad band observations are needed to constrain the full set of physical parameters of NGC 5055 X-1.

Acknowledgements. We thank the anonymous referee for useful comments that have helped to improve the manuscript. The authors also thank Aneta Siemiginowska for insights into *Chandra* data reduction process. AR was supported by Polish National Science Center grants No. 2015/17/B/ST9/03422,

2015/18/M/ST9/00541. BDM acknowledges support from the European Union's Horizon 2020 research and innovation programme under the Marie Skłodowska-Curie grant agreement No. 798726. The work has made use of publicly available data from HEASARC Online Service, Chandra Interactive Analysis of Observations (CIAO) developed by Chandra X-ray Center, Harvard & Smithsonian center for astrophysics (USA), and the XMM-Newton Science Analysis System (SAS) developed by European Space Agency (ESA).

References

- Abramowicz, M. A., Czerny, B., Lasota, J. P., & Szuszkiewicz, E. 1988, *ApJ*, 332, 646
- Arnaud, K. A. 1996, *Astronomical Society of the Pacific Conference Series*, Vol. 101, *XSPEC: The First Ten Years*, ed. G. H. Jacoby & J. Barnes, 17
- Bachetti, M., Harrison, F. A., Walton, D. J., et al. 2014, *Nature*, 514, 202
- Cao, X. 2009, *MNRAS*, 394, 207
- Carpano, S., Haberl, F., Maitra, C., & Vasilopoulos, G. 2018, *MNRAS*, 476, L45
- Colbert, E. J. M. & Mushotzky, R. F. 1999, *ApJ*, 519, 89
- Devi, A. S., Misra, R., Agrawal, V. K., & Singh, K. Y. 2007, *ApJ*, 664, 458
- Done, C. & Kubota, A. 2006, *MNRAS*, 371, 1216
- Fabbiano, G. 1989, *ARA&A*, 27, 87
- Feng, H. & Kaaret, P. 2006a, *ApJ*, 653, 536
- Feng, H. & Kaaret, P. 2006b, *ApJ*, 650, L75
- Feng, H. & Kaaret, P. 2007, *ApJ*, 660, L113
- Feng, H. & Kaaret, P. 2009, *ApJ*, 696, 1712
- Fürst, F., Walton, D. J., Harrison, F. A., et al. 2016, *ApJ*, 831, L14
- Fürst, F., Walton, D. J., Stern, D., et al. 2017, *ApJ*, 834, 77
- Gierliński, M. & Done, C. 2004, *MNRAS*, 347, 885
- Gladstone, J. C., Roberts, T. P., & Done, C. 2009, *MNRAS*, 397, 1836
- Gregory, P. C. & Loredo, T. J. 1992, *ApJ*, 398, 146
- Gronkiewicz, D. & Różańska, A. 2020, *A&A*, 633, A35
- Heida, M., Jonker, P. G., Torres, M. A. P., et al. 2016, *MNRAS*, 459, 771
- Heida, M., Torres, M. A. P., Jonker, P. G., et al. 2015, *MNRAS*, 453, 3510
- HI4PI Collaboration, Ben Bekhti, N., Flöer, L., et al. 2016, *A&A*, 594, A116
- Hirano, A., Kitamoto, S., Yamada, T. T., Mineshige, S., & Fukue, J. 1995, *ApJ*, 446, 350
- Huppenkothen, D., Bachetti, M., Stevens, A. L., et al. 2019, *ApJ*, 881, 39
- Israel, G. L., Belfiore, A., Stella, L., et al. 2017a, *Science*, 355, 817
- Israel, G. L., Papitto, A., Esposito, P., et al. 2017b, *MNRAS*, 466, L48
- Kaaret, P., Corbel, S., Prestwich, A. H., & Zezas, A. 2003, *Science*, 299, 365
- Kaaret, P., Feng, H., & Roberts, T. P. 2017, *ARA&A*, 55, 303
- Kajava, J. J. E. & Poutanen, J. 2009, *MNRAS*, 398, 1450
- Kajava, J. J. E., Poutanen, J., Farrell, S. A., Grisé, F., & Kaaret, P. 2012, *MNRAS*, 422, 990
- King, A. R. 2009, *MNRAS*, 393, L41
- King, A. R., Davies, M. B., Ward, M. J., Fabbiano, G., & Elvis, M. 2001, *ApJ*, 552, L109
- King, A. R. & Puchnarewicz, E. M. 2002, *MNRAS*, 336, 445
- Kubota, A., Ebisawa, K., Makishima, K., & Nakazawa, K. 2005, *ApJ*, 631, 1062
- Kubota, A. & Makishima, K. 2004, *ApJ*, 601, 428
- McQuinn, K. B. W., Skillman, E. D., Dolphin, A. E., Berg, D., & Kennicutt, R. 2017, *AJ*, 154, 51
- Middleton, M. J., Walton, D. J., Roberts, T. P., & Heil, L. 2014, *MNRAS*, 438, L51
- Miller, J. M., Fabbiano, G., Miller, M. C., & Fabian, A. C. 2003, *ApJ*, 585, L37
- Miller, J. M., Fabian, A. C., & Miller, M. C. 2004a, *ApJ*, 614, L117
- Miller, J. M., Fabian, A. C., & Miller, M. C. 2004b, *ApJ*, 607, 931
- Mineshige, S., Hirano, A., Kitamoto, S., Yamada, T. T., & Fukue, J. 1994, *ApJ*, 426, 308
- Mondal, S., Belczyński, K., Wiktorowicz, G., Lasota, J.-P., & King, A. R. 2020, *MNRAS*, 491, 2747
- Motch, C., Pakull, M. W., Grisé, F., & Soria, R. 2011, *Astronomische Nachrichten*, 332, 367
- Motch, C., Pakull, M. W., Soria, R., Grisé, F., & Pietrzyński, G. 2014, *Nature*, 514, 198
- Petrucci, P. O., Gronkiewicz, D., Rozanska, A., et al. 2020, *A&A*, 634, A85
- Pinto, C., Middleton, M. J., & Fabian, A. C. 2016, *Nature*, 533, 64
- Roberts, T. P. & Warwick, R. S. 2000, *MNRAS*, 315, 98
- Roberts, T. P., Warwick, R. S., Ward, M. J., & Goad, M. R. 2004, *MNRAS*, 350, 1536
- Różańska, A., Bresler, K., Beldycki, B., Madej, J., & Adhikari, T. P. 2018, *A&A*, 612, L12
- Shakura, N. I. & Sunyaev, R. A. 1973, *A&A*, 24, 337
- Singha, A. C. & Devi, A. S. 2019, *Acta Astron.*, 69, 339
- Skipper, C. J. & McHardy, I. M. 2016, *MNRAS*, 458, 1696
- Stobart, A. M., Roberts, T. P., & Wilms, J. 2006, *MNRAS*, 368, 397
- Sutton, A. D., Roberts, T. P., & Middleton, M. J. 2013, *MNRAS*, 435, 1758
- Swartz, D. A., Soria, R., Tennant, A. F., & Yukita, M. 2011, *ApJ*, 741, 49
- Tikhonov, N. A., Lebedev, V. S., & Galazutdinova, O. A. 2015, *Astronomy Letters*, 41, 239
- Tully, R. B., Courtois, H. M., Dolphin, A. E., et al. 2013, *AJ*, 146, 86
- Watarai, K.-y., Fukue, J., Takeuchi, M., & Mineshige, S. 2000, *PASJ*, 52, 133
- Zdziarski, A. A., Johnson, W. N., & Magdziarz, P. 1996, *MNRAS*, 283, 193
- Zycki, P. T., Done, C., & Smith, D. A. 1999, *MNRAS*, 309, 561